THE JOURNAL OF PHYSICAL CHEMISTRY C

Article

pubs.acs.org/JPCC

# Tailoring the Structural, Optical, and Photoluminescence Properties of Porous Silicon/$TiO_2$ Nanostructures

Igor Iatsunskyi,*[,†,‡] Mykola Pavlenko,[‡] Roman Viter,[‡,§] Mariusz Jancelewicz,[†] Grzegorz Nowaczyk,[†] Ieva Baleviciute,[∥] Karol Załęski,[†] Stefan Jurga,[†] Arunas Ramanavicius,[∥] and Valentyn Smyntyna[‡]

[†]NanoBioMedical Centre, Adam Mickiewicz University, 85 Umultowska Str., 61-614 Poznan, Poland

[‡]Department of Experimental Physics, Odessa National I.I. Mechnikov University, 42 Pastera Str., 65023 Odessa, Ukraine

[§]Institute of Atomic Physics and Spectroscopy, University of Latvia, 19 Raina Boulevard, LV 1586 Riga, Latvia

[∥]Department of Chemistry Vilnius University, 24 Naugarduko Str., LT-03225 Vilnius, Lithuania

Supporting Information

**ABSTRACT:** The structural, optical, and photoluminescence properties of porous silicon (PSi)/titanium dioxide ($TiO_2$) nanostructures were investigated. PSi structures consisting of macro- and mesoporous layers were fabricated by metal-assisted chemical etching, and then $TiO_2$ was introduced inside the PSi matrix using the atomic layer deposition technique. We performed scanning electron microscopy, transmission electron microscopy (TEM), X-ray diffraction, energy dispersive X-ray spectroscopy, Raman spectroscopy, ellipsometry, and photoluminescence (PL) spectroscopy to characterize the prepared and annealed PSi/$TiO_2$ nanostructures. TEM and Raman analyses revealed that $TiO_2$ had a crystalline anatase structure. PL measurements of the PSi/$TiO_2$ composite system showed two broad peaks at approximately 2.4−3 eV (blue PL) and 1.7−1.9 eV (red PL). The mechanisms of the emissions were discussed, and it was found that two main competing recombination mechanisms take place, including radiative recombination through the surface states (surface recombination) and through oxygen vacancies and self-trapped excitons (volume recombination).

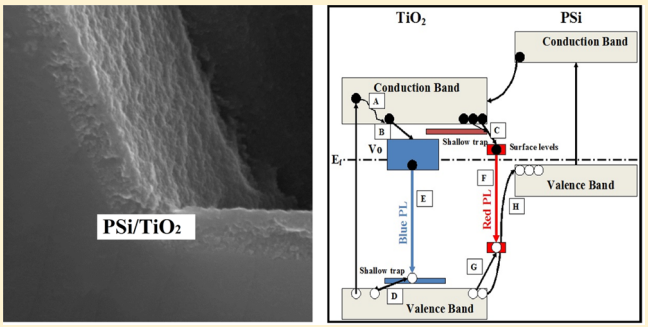


## 1. INTRODUCTION

Porous silicon (PSi) and PSi nanostructures based on PSi/$TiO_2$ have drawn increased attention for use in various applications, such as photovoltaics,[1,2] photoelectrochemical water splitting,[3−5] gas sensors,[6] Li-ion batteries,[7−9] and so forth. Nanostructures based on Si−$TiO_2$ show improved photocatalytic efficiency due to their enhanced separation of excited electrons and holes. PSi nanostructures also exhibit great potential in optical biosensor applications due to the possible tuning of a refractive index that can used for the detection of biological substances or chemical vapors.[10,11] It is well-known that depending on the pore size PSi could be very efficiently detect molecules and other bio-agents comparable in size to the pore diameter. Therefore, the simultaneous use of two or more PSi layers (macro-, meso-, and/or micro-PSi) allows us to produce sensitive biosensors capable of detecting various types of molecules. Furthermore, PSi nanostructures are favorable because of the low cost of silicon and their compatibility with the modern integrated circuit (IC) industry. Undoubtedly, the improvement in electro-optical properties is dependent on the microstructure of the nanostructure. In this regard, studies on the morphology and physical properties of nanostructures has gained increasing attention in recent years.

In the present study, we report the structural and optical properties of the PSi/$TiO_2$ composite system. Metal-assisted chemical etching (MACE) is the most preferable method to fabricate PSi structures possessing different porosities and morphologies.[12] Here, PSi possesses two types of porosity, incuding a first level macroporous structure and second level mesoporous structure. $TiO_2$ was introduced inside the PSi matrix to fabricate the PSi/$TiO_2$ nanostructure. For this purpose, we used the atomic layer deposition (ALD) technique. ALD is a deposition process for highly uniform and conformal thin films. Because of the self-limiting reaction in the ALD process, films that are very conformal with thicknesses that are precisely controlled could be grown over large areas, even inside the PSi.[13,14] The morphology and phase structure were detected by scanning and transmission electron microscopy (SEM, TEM), X-ray diffraction (XRD), energy dispersive X-ray spectroscopy (EDX), and Raman spectroscopy. Optical properties have been analyzed by means of ellipsometry. In this paper, we also concentrated on the broad photoluminescence (PL) bands in the visible spectral region. Analysis of the PL spectra

**Received:** December 22, 2014
**Revised:** March 16, 2015





DOI: 10.1021/acs.jpcc.5b01670
J. Phys. Chem. C XXXX, XXX, XXX−XXX

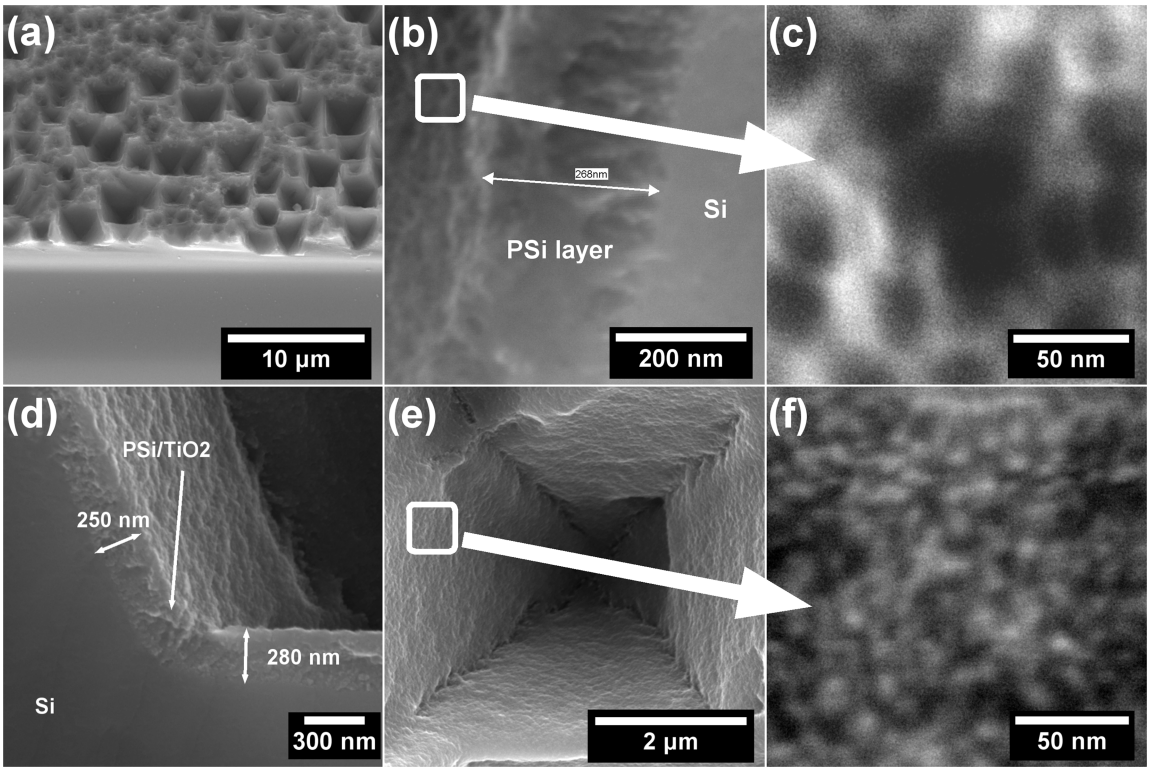


**Figure 1.** Cross-sectional view of SEM images of a (a) macroporous silicon surface fabricated by MACE, (b) mesoporous layer of PSi, and (c) mesoporous silicon surface (high magnification). (d) Cross-sectional view of prepared PSi/$TiO_2$ nanostructure after 150 ALD cycles. (e) Planar view SEM image of an individual macropore in the PSi/$TiO_2$ nanostructure after 150 ALD cycles. (f) Surface of the macropore in the PSi/$TiO_2$ nanostructure (high magnification).

indicates PL quenching due to electron−hole separation at the PSi/$TiO_2$ heterojunction. Mechanisms of the PL emissions, along with structural and optical changes induced by annealing, will be discussed.

## 2. EXPERIMENTAL SECTION

**Preparation of PSi.** The PSi samples were fabricated from (100) oriented and highly doped p-type Si (B-doped, $q < 0.005$ Ω cm) utilizing MACE.[12] Silicon samples (1 × 1 cm), after standard RCA cleaning, were cleaned with acetone, isopropanol, and deionized water via ultrasonic cleaning. The silver particles, which act as catalysts to assist in the etching of silicon, were deposited on Si samples by immersion in 0.2 M HF and $10^{-3}$ M $AgNO_3$ metallization aqueous solutions. The time of immersion was 60 s. Then, the samples were etched in aqueous solutions containing HF (40%), $H_2O_2$ (30%), and ultrapure $H_2O$ at a ratio of 80:80:20 $H_2O_2$/$H_2O$/HF for 60 min. After etching, the samples were dipped in $HNO_3$ solution to remove the silver particles for 30 min and were then dipped in HF (5%) solution to remove oxide. They were then cleaned with deionized water and blown dry with nitrogen. The etching and immersion procedures were performed at room temperature.

**ALD Coating.** The PSi samples were placed in an ALD reactor (Picosun). The $TiO_2$ thin films were deposited onto the PSi substrates using $TiCl_4$ and water as ALD precursors. Nitrogen ($N_2$) flow was used as a carrier and purging gas. $TiCl_4$ precursor and water were evaporated at 20 °C. In this study, the standard cycle consisted of a 0.1 s $TiCl_4$ exposure, a 3 s $N_2$ purge, a 0.1 s exposure to water, and a 4 s $N_2$ purge. The total flow rate of $N_2$ was 150 standard cubic centimeters per minute (sccm). $TiO_2$ thin films were grown at 300 °C. The growth rate was typically 0.5 Å per cycle for $TiO_2$ on the planar silicon surface. The growth per cycle was controlled by measuring the films thickness on Si-wafer reference substrates placed in the reactor. After $TiO_2$ deposition, some samples were annealed at 400 °C for an hour in an ambient atmosphere.

**Material Characterization and Optical Measurements.** Structural properties of PSi and ALD $TiO_2$ thin films were investigated by X-ray diffraction (XRD) (Empyrean diffractometer), scanning electron microscopy (SEM) (JEOL, JSM-7001F) with an energy dispersive X-ray (EDX) analyzer, transmission electron microscopy (TEM) (JEOL ARM 200F high-resolution transmission electron microscope (200 kV) with EDX analyzer), and Raman scattering (Renishaw micro-Raman spectrometer equipped with a confocal microscope (Leica) and laser ($\lambda_{excitation}$ = 514 nm). The cross sections and lamellas for TEM investigations were prepared by Focused Ion Beam (JEOL, JIB-4000).

Optical properties of the samples have been studied by photoluminescence spectroscopy and ellipsometry measurements. Ellipsometry spectroscopy was used to obtain optical constants of PSi and $TiO_2$ thin films deposited on Si substrates. Semilab GES5E spectroscopic ellipsometer (extended visible: 1.23−5 eV). The ellipsometric measurements were carried out at a fixed incident angle of 75°, close to the Brewster's angle for a silicon substrate, and a variable wavelength between 300 nm and 1 μm. Then, the experimental tan ($\psi$) and cos ($\delta$) data were fitted using WinElli II software using a single layer $TiO_2$ adjusted model to obtain the film thicknesses with a goodness of fit over 0.999 in the full wavelength range. Photoluminescence (PL) of the samples was measured at room temperatures using a homemade setup. The excitation of PL


DOI: 10.1021/acs.jpcc.5b01670
J. Phys. Chem. C XXXX, XXX, XXX−XXX

was performed with a nitrogen laser (337.7 nm), and the emission spectra were recorded in the range of 400−850 nm.

## 3. RESULTS AND DISCUSSION

**Structural Characterization.** Figure 1a shows the SEM image of macroporous silicon (macro-PSi) obtained by MACE. The cross-sectional SEM view of the PSi shows the presence of nearly pyramid-shaped pores (macropores) propagating into the bulk from the surface in a perpendicular manner. The average pore size (diagonal) is approximately 3−5 $\mu$m, and the thickness of the macro-PSi layer is ∼1.5 $\mu$m. The surface of an individual macropore consists of a mesoporous silicon (meso-PSi) layer with a thickness ranging from 200 to 300 nm (Figure 1b). The thickness of the bottom layer of the pore is bigger than the sidewall (Figure 1d). Formation of this complex porous structure can be explained by the model proposed by Chartier et al. where etching occurs at the pore walls (pore widening) and tips (pore deepening) due to injected holes, which may diffuse away from the pore tip along the pore walls.[15] Figure 1c shows that the layer of meso-PSi consists of a large number of small pores. The average pore size is approximately 15−30 nm (Figure 1c).

Cross-sectional SEM images indicate that $TiO_2$ infiltrates and conformally coats the mesopores (Figure 1d). EDX measurements were carried out to evaluate the chemical composition of PSi/$TiO_2$ and the distribution of titanium and oxygen atoms inside the porous structure. EDX confirms that PSi contains Ti, O, and Si not only on the top of the film but also within the porous matrix (not shown here). Figure 1e shows a planar SEM image of an individual macropore of PSi/$TiO_2$ after 150 ALD cycles. The image shows that the inner surface of the macropore is quite rough. After the ALD process, the surface of the PSi layer consists of spherical grains uniformly distributed over the surface (Figure 1f). Depending on the number of ALD cycles, a typical grain ranged from 20 to 40 nm in size.

Figure 2a shows a TEM image of the PSi after 200 ALD cycles. The thickness of the layer is ∼240 nm. We noticed that the upper layer (40−60 nm from the top) of the meso-PSi has a higher density, probably due differences in the porosity. EDX analysis of this sample is shown in Figure 2b. The EDX profile image confirms that the Ti and O atoms quite uniformly penetrate into the meso-PSi matrix. Opposite to the deposition of films on flat surfaces, the precursor molecules have to diffuse into a porous structure. During the ALD process, molecules of precursors penetrate into the pore, forming the layer or other structures of $TiO_2$ inside the PSi matrix.

High-resolution TEM (HRTEM) image of the PSi/$TiO_2$ nanostructure is shown in Figure 2c. Using ImageJ software, the grain size and interplanar distances were calculated (Figure 2c, d). HRTEM image shows the formation of crystallites in the PSi matrix (Figure 2c). Lattice fringes are clearly visible, which prove crystallinity of the particles obtained. We determined the interplanar distances of 0.34 and 0.20 nm for anatase and 0.27, 0.16, and 0.13 nm for silicon, which correspond to lattice distances of (101) and (004) planes of anatase and (200), (311), and (200) planes of silicon, respectively. The interplanar distance for the (101) lattice plane was lower than that for anatase $TiO_2$ as reported in the Joint Committee on Powder Diffraction Standards (JCPDS) database (0.352 nm). The decrease in the interplanar distance could be due to lattice strain effects. The average grain size of anatase varied from 6 ± 2 nm to 9 ± 2 nm for 150 and 200 ALD cycles, respectively. It

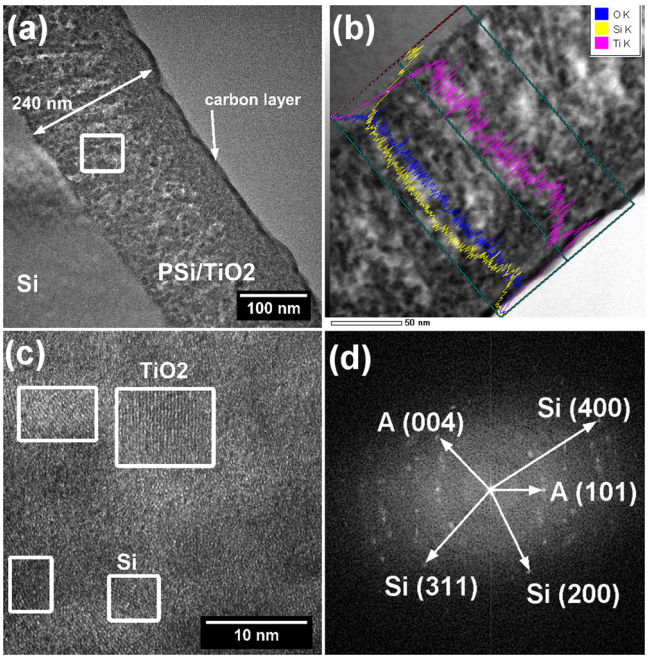


**Figure 2.** (a) Cross-sectional TEM image of PSi-$TiO_2$ after 200 ALD cycles. (b) EDX profile analysis. (c) HRTEM image of the area highlighted with a white square in (a). (d) Inverse fast Fourier transform of the area highlighted with a white square in the HRTEM image (a). "A" can be identified as anatase.

was difficult to identify any individual grains corresponding to anatase for the samples prepared with 100 ALD cycles. Some heterojunctions of anatase $TiO_2$ and Si were also observed by HRTEM.

To confirm the composition of PSi/$TiO_2$, Raman spectroscopy (Figure 3) and XRD (not reported here) have been used. Raman spectra of the prepared PSi/$TiO_2$ showed no significant peaks of $TiO_2$ in the background of the strong spectrum of PSi, indicating that the prepared $TiO_2$ was amorphous (Figure 3a). Upon increasing the number of ALD cycles, the peaks corresponding to PSi become weaker due to high absorbance of the amorphous $TiO_2$ layer covering the PSi. A Raman peak at 146 $cm^{-1}$, corresponding to the anatase phase of $TiO_2$, can clearly be observed after annealing at 400 °C for 1 h in air, suggesting that the prepared amorphous phase crystallizes to anatase $TiO_2$ (Figure 3b). This is typical of the anatase $TiO_2$ phase, but the peak is broader and blue-shifted with respect to bulk anatase (peak position is 144 $cm^{-1}$ and full width at half-maximum (fwhm) is 7 $cm^{-1}$). The broadening and blue-shift of the Raman peaks are attributed to phonon confinement effects that usually exist in nanomaterials.[16−19] Upon increasing the number of ALD cycles, the intensity of the anatase Raman peak increases. A simple confinement model may be used to calculate the shape of the anatase mode at various nanocrystal sizes ($L$).[18,19] In this model, the Raman spectrum is given by

$$I(\omega) \cong \int_{BZ} \frac{d^3q\,|C(0,q)|^2}{(\omega - \omega(q))^2 - \left(\frac{\Gamma_0}{2}\right)^2} \quad (1)$$

where $|C(0,q)|^2 = \exp(-q^2L^2/(16\pi^2))$, $\Gamma_0$ is the natural line width, $\omega(q)$ is the dispersion relation for optical phonons, and $\omega$ and $q$ are the frequency and wavevector, respectively. The anatase Raman peaks are centered at 147 $cm^{-1}$ (100 and 150 ALD cycles) and 146 $cm^{-1}$ (200 cycles) with fwhm of 25, 24,



DOI: 10.1021/acs.jpcc.5b01670
J. Phys. Chem. C XXXX, XXX, XXX−XXX

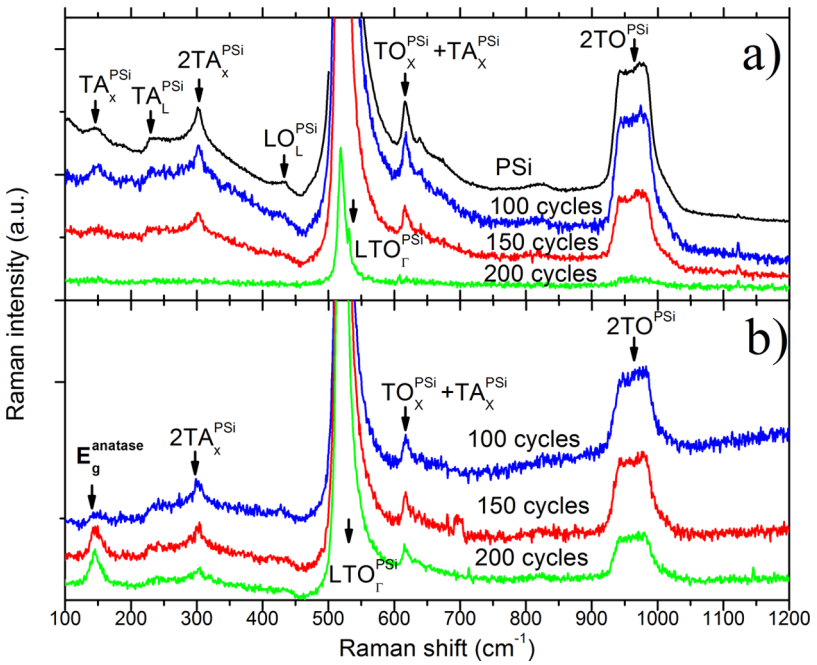


**Figure 3.** (a) Raman spectra of prepared PSi/$TiO_2$ nanostructures and PSi. The arrows indicate the Raman modes of the PSi. (b) Raman spectra of PSi/$TiO_2$ nanostructures annealed at 400 °C. The arrows indicate the Raman modes of PSi and anatase.

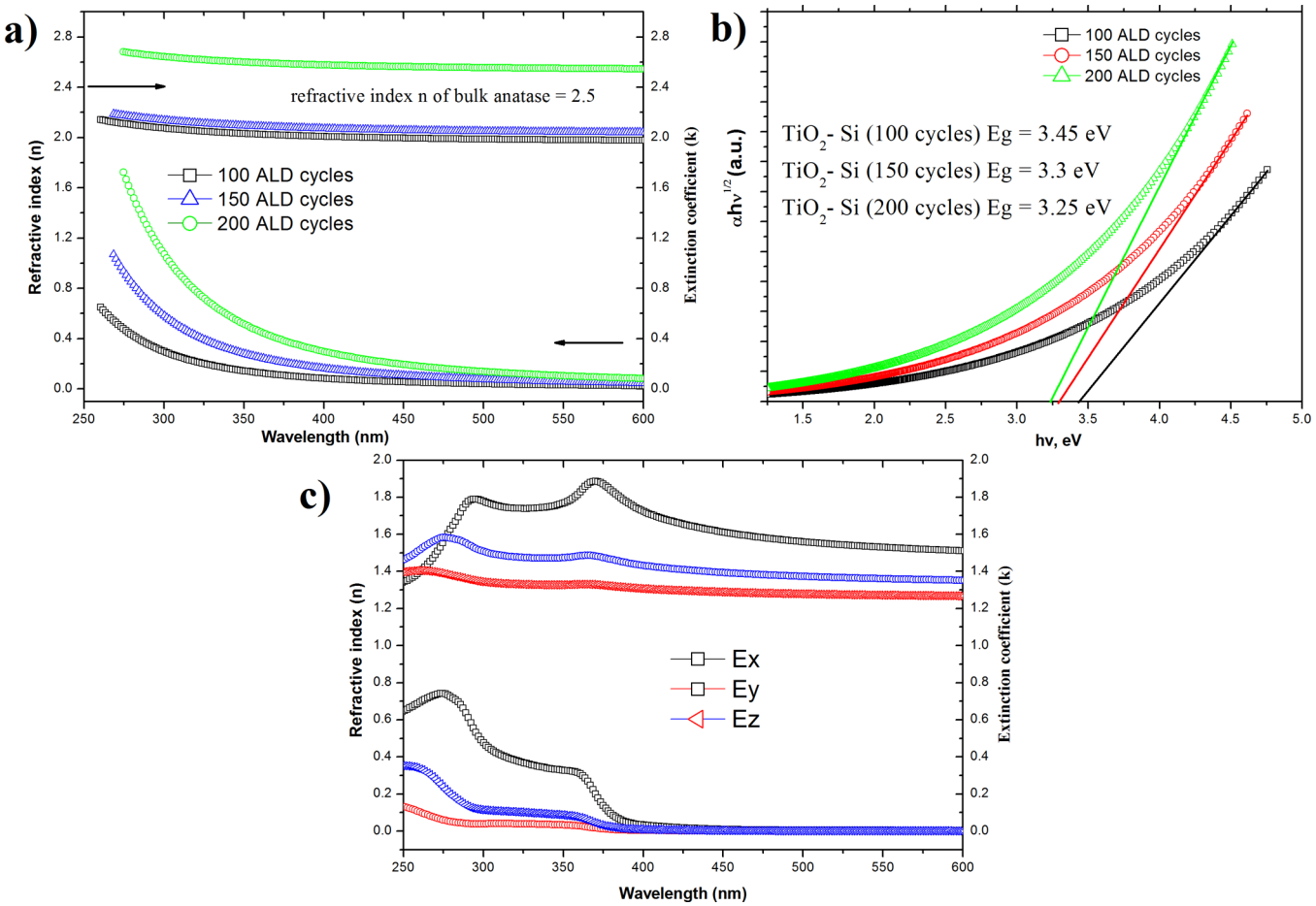


**Figure 4.** (a) Refractive index ($n$) and extinction coefficient ($k$) of $TiO_2$−Si with differing numbers of ALD cycles. (b) Band gap estimation of $TiO_2$−Si with differing numbers of ALD cycles. (c) Refractive index ($n$) and extinction coefficient ($k$) of PSi. $E_X$, $E_Y$, and $E_Z$ are components of the electric field vector.



DOI: 10.1021/acs.jpcc.5b01670
J. Phys. Chem. C XXXX, XXX, XXX−XXX

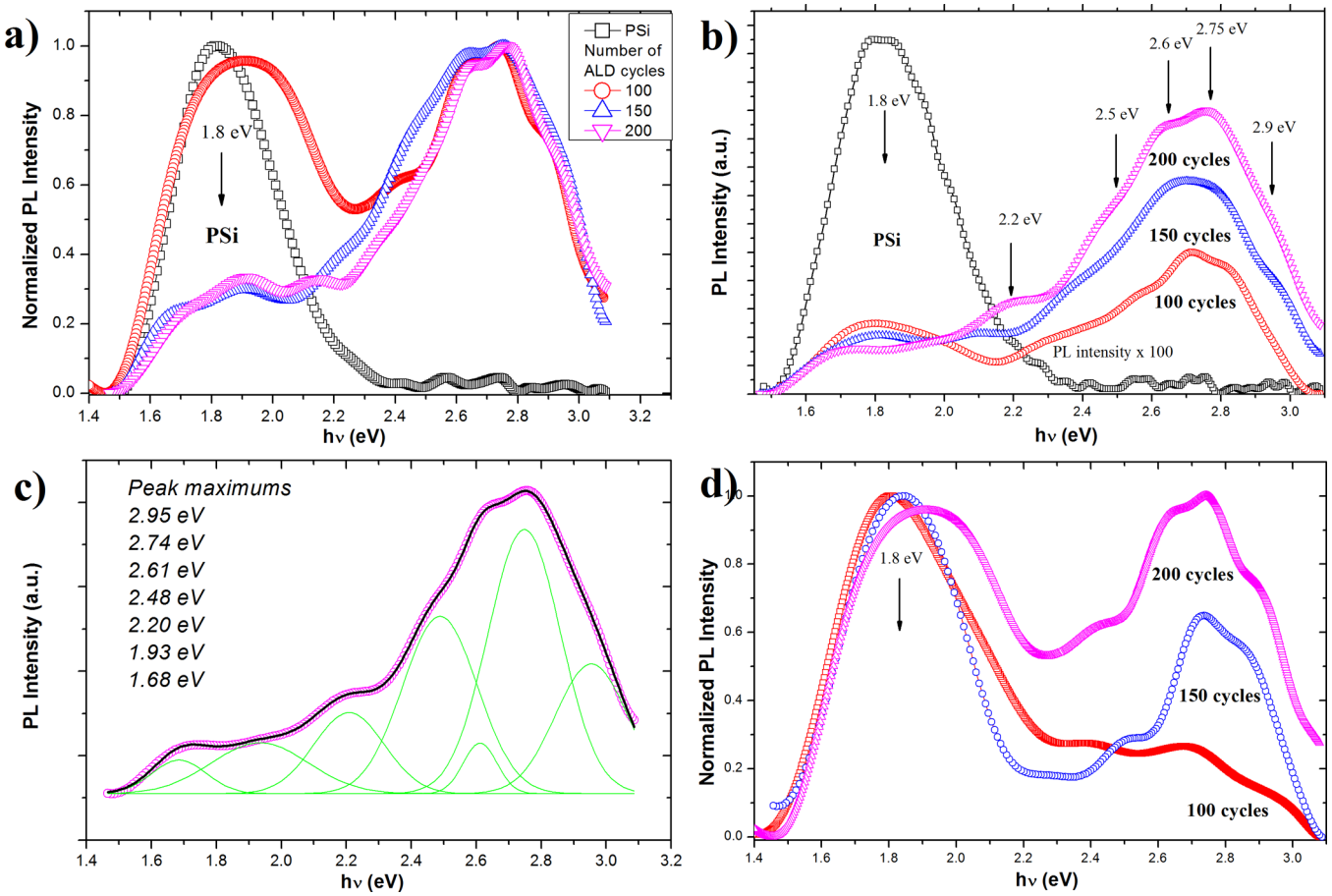


**Figure 5.** PL spectra of PSi and PSi/$TiO_2$ nanostructures with differing numbers of ALD cycles (a) as prepared, (b) as annealed, and (c) with curve fitting of the PL spectrum (PSi/$TiO_2$ nanostructure, 200 ALD cycles). (d) Normalized PL spectra of $TiO_2$−Si with differing numbers of ALD cycles.

and 23 $cm^{-1}$ deposited by 100, 150, and 200 cycles, respectively. These correspond to crystal sizes of approximately 5, 6, and 7.8 nm, respectively. Comparing these results with TEM findings, we can conclude that a very small amount of anatase nanocrystals have formed in the prepared PSi/$TiO_2$ composites. Annealing of these samples leads to amorphous-to-crystalline phase transitions. However, we could observe the anatase peak at 146 $cm^{-1}$ for the prepared $TiO_2$ layer grown on the planar silicon surface (Figure S4, Supporting Information). This indicates that the mean crystallite size and the crystallinity of the ALD $TiO_2$ are influenced dramatically by the morphology of the substrate. In the case of the porous structure, additional thermal treatment is needed to form anatase crystals inside the PSi matrix.

**Optical and PL Properties.** $TiO_2$ layers were deposited on a silicon substrate in similar conditions in the same environment for optical measurements. The extinction coefficient ($k$) and refractive index ($n$) of ALD-deposited $TiO_2$ on the planar silicon surface and PSi nanolayers were calculated to be in the range of 260−1000 nm using the ellipsometry technique. It should be noted that it was impossible to calculate $n$ and $k$ for the PSi/$TiO_2$ nanostructures due to high light scattering. The spectral dependence of the extinction coefficient of the $TiO_2$ nanolayers is shown in Figure 4a. It can be seen that the extinction coefficient value increased with the number of ALD cycles. The absorption edge of the samples laid in the range of 260−400 nm, which is typical of $TiO_2$ nanostructures.

Band gap values of $TiO_2$ nanostructures from ellipsometry data were estimated.[20−22] Extinction coefficient $k$ and absorption coefficient $\alpha$ are related according to the following equation[20]

$$\alpha = \frac{4\pi k}{\lambda} \tag{2}$$

where $\lambda$ is wavelength.

Because $TiO_2$ is an n-type semiconductor with indirect optical transitions, the relationship between band gap $E_g$ and absorption coefficient $\alpha$ can be described by the following equation[23]

$$(\alpha \times h\nu)^{1/2} \sim (h\nu - E_g) \tag{3}$$

where $h\nu$ is photon energy.

The spectra dependence of the absorption data is plotted in specific coordinates in Figure 4b. It can be seen that the absorption edge demonstrated a blue-shift with a decreased number of ALD cycles. Using eq 3, the band gap values were determined graphically.[21,22,24] The obtained values were 3.45, 3.3, and 3.25 for $TiO_2$ nanolayers deposited by 100, 150, and 200 cycles, respectively. The band gap value of bulk $TiO_2$ (anatase) is ∼3.2 eV. The ALD-deposited $TiO_2$ nanolayers showed higher values of $E_g$, which could refer to the quantum confinement effect, that were affected by low grain size values.[20−23] These results have been confirmed by Raman spectroscopy (Figure S3, Supporting Information).



DOI: 10.1021/acs.jpcc.5b01670
J. Phys. Chem. C XXXX, XXX, XXX−XXX

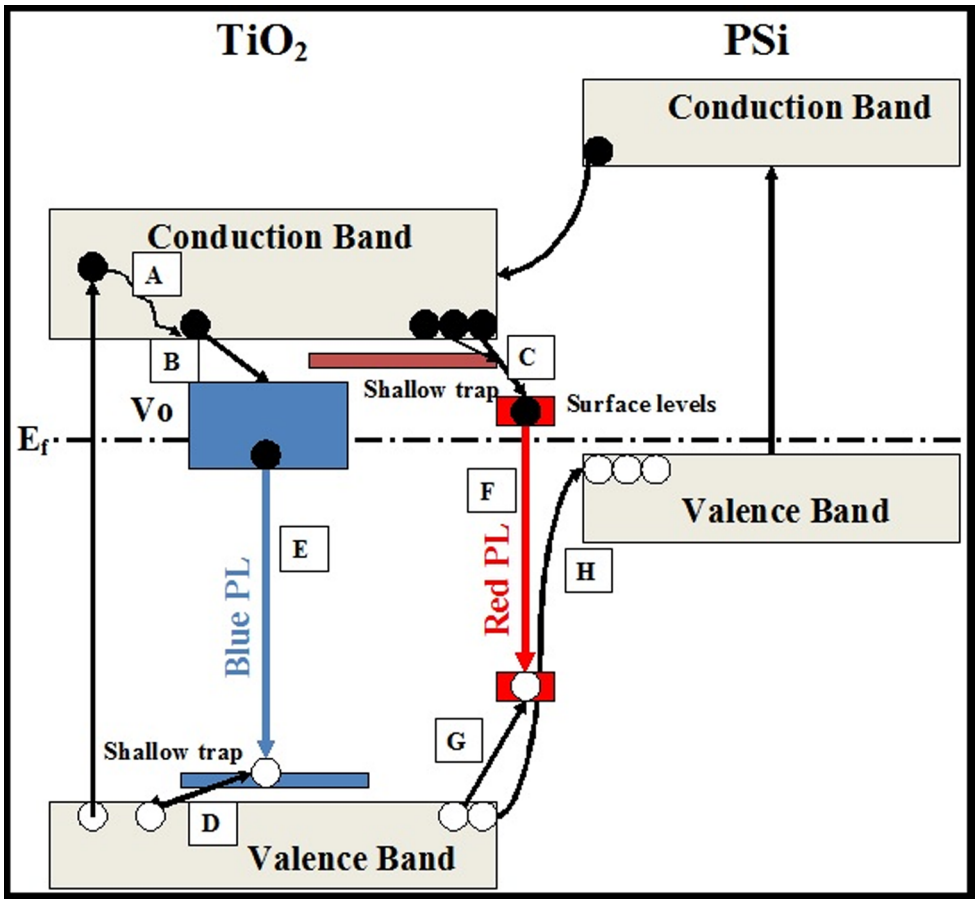


**Figure 6.** Schematic illustration of the relaxation processes of the photogenerated carriers in PSi/$TiO_2$. Electrons (black circle), holes (white circle), and oxygen vacancies ($V_O$) band. Processes: (A) electrons quenched to the bottom of the CB, (B) electrons captured by deep traps, (C) electrons captured by surface traps, (D) holes captured by shallow traps, (G) holes captured by surface traps, (E) blue luminescence emission, (F) red luminescence emission, and (H) hole injection from $TiO_2$ to PSi.

The dependence of the refractive index on the wavelength is also shown in Figure 4a. The refractive index value is drastically increased for $TiO_2$ nanolayers deposited by 200 ALD cycles. The refractive index of the thin film could differ from their structural properties.[20,24] Previously, we had demonstrated a complex analysis of optical constants of ZnO/$Al_2O_3$ nanolaminates with different thicknesses of a single layer.[20] It was shown that the refractive index of the ZnO layers increased with the thickness. The increase in the refractive index was explained by the increase in the packing density of thicker layers, which was confirmed by analysis of the structural properties.[20,24]

The investigated $TiO_2$ films showed a decreased band gap value with increased thickness, which means that the crystalline structure of the samples was transformed from nanostructured to bulk-like. Therefore, according to refs 20 and 24, the packing density of the films should increase, explaining the behavior of $n(\lambda)$ dependence. Low values of the refractive index for thinner samples can be explained by the cluster-like structure or lower crystalline quality. However, as the films were deposited on the planar silicon surface at 300 °C, the operating temperature was enough for amorphous-to-crystalline phase transitions in the $TiO_2$ samples, which were confirmed by TEM and Raman spectroscopy (Figures S3 and S4, respectively, Supporting Information). Thus, the optical properties of the deposited $TiO_2$ samples are tailored by their structural parameters.

The spectral dependence of the extinction coefficient and the refractive index of the PSi are shown in Figure 4c, where the optical anisotropy of the PSi layer can be clearly seen. It is well-known that the PSi layer is composed of air and silicon. Therefore, its refractive index should range from 1.0 (refractive index of air) to 3.4 (refractive index of pure silicon) depending on its porosity.[25] Taking into account the values of the refractive index, we conclude that the porosity of the PSi layer has a range[25,26] of 75−85%.

As is well-known, the absorption spectrum of PSi is the sum of the different microscopic absorption processes. Absorption measurements are often complicated by difficulties in interpretation that arise from the inhomogeneity of PSi. However, what is clear from the absorption studies is that the spectra are shifted toward higher energy compared to that of bulk Si, which could refer to the quantum confinement effect. Using eq 2, the band gap of PSi was estimated, and the experimental $E_g$ of the film is approximately 2.3−2.8 eV.

Photoluminescence measurements were performed to understand the presence of defects and recombination ability of charge carriers. $TiO_2$ introduced into the PSi matrix may change the surface structure and interface between $TiO_2$ and PSi. It is generally believed that visible emissions from $TiO_2$ films are mainly due to self-trapped excitons (STEs), oxygen vacancies ($V_O$), and surface states.

The PL of PSi, $TiO_2$−Si, and PSi/$TiO_2$ nanostructures were measured in the region of light wavelengths from 400 to 900


DOI: 10.1021/acs.jpcc.5b01670
J. Phys. Chem. C XXXX, XXX, XXX−XXX

nm (Figure 5). The maximum of the PL peak for PSi was detected at 1.8 eV (690 ± 5 nm). After ALD deposition of $TiO_2$ on PSi, PL was investigated, and the PL spectra showed two broad peaks at approximately 2.4−3 eV (blue PL) and 1.7−1.9 eV (red PL) (Figure 5a, b). However, after the deposition of $TiO_2$, the PL intensity is degraded dramatically. This might indicate that the PSi/$TiO_2$ nanostructure had a lower recombination rate. We suggest that the PSi/$TiO_2$ heterojunctions separate the photogenerated charge carriers due to a difference in the energy levels of their conduction bands (CB) and valence bands (VB) (shown later in Figure 6).

After multipeak Gaussian fitting of the annealed PSi−$TiO_2$ PL spectrum, we obtained seven PL bands (Figure 5c). The PL band at 2.95 eV corresponds to the STEs localized on the $TiO_6$ octahedral.[27−31] The bands at 2.74 and 2.48 eV are attributed to oxygen vacancies with two electrons[27,32−34] and one electron, respectively.[27,32] The PL band at 2.61 eV probably originates from surface Ti−OH bonds[30,35] or from neutral oxygen vacancy.[32,36]The band at 2.2 eV can be assigned to the trap level related to oxygen vacancies on the surface.[30,37] The peaks at 1.93 and 1.63 eV more likely originate from the surface states.[38−40] Zhang et al. have shown that the surface states responsible for the red PL are likely to be formed by some unsaturated surface atoms of $TiO_2$ nanocrystallites[39] related to $Ti^{4+}$, $Ti^{3+}$, and $Ti^{2+}$.

Comparing prepared and annealed samples, we can conclude that two primary competing recombination mechanisms take place: radiative recombination through the surface states (surface recombination) corresponding to the red PL and radiative recombination through the oxygen vacancies ($V_O$) and STE (volume recombination) corresponding to the blue PL. Thus, both the volume and surface area affect the intensity of the PL spectrum. However, when the amount of materials was decreased, the ratio of the surface area to volume was also increased, and the surface factor becomes a more important characteristic to the material's optical and PL properties (Figure 5d). Thus, the former mechanism should be crucial for $TiO_2$ with a high concentration of surface defects, which is typical for amorphous or low crystalline quality materials. After annealing, the crystallinity becomes very high, and the specific surface area decreases. Thus, when the number of defect states is decreased, the latter mechanism prevails over the former, and radiative recombination occurs through oxygen vacancies.

Figure 6 shows the simple scheme of possible relaxation processes in PSi/$TiO_2$. Laser excitation at 337 nm excites the electrons to the upper CB and then excited electrons are quenched to the bottom CB (process A, Figure 6). Because of the presence of oxygen vacancies, the electrons do not directly recombine with holes in the VB. Instead, they are captured by the oxygen vacancies and then recombine with the holes in the VB (process B, Figure 6), accompanying radiative emission corresponding to the blue PL (process E, Figure 6). As was shown by Wang et al., some carriers (electrons and/or holes) are first captured by shallow defect states and then quenched to the luminescent sites through trap-to-trap hopping to finally produce visible luminescence.[40] On the other hand, photogenerated electrons and holes could be trapped by the surface states (processes C and G, Figure 6) and then recombine with emission corresponding to the red PL (process F, Figure 6).

It is well-known that reducing photogenerated charge carrier recombination in heterojunctions improves photocatalytic activity.[1−5] Because of the difference in the energy level of CB and VB at the PSi-$TiO_2$ interface, separation of the photogenerated electrons and holes occurs very fast, reducing recombination of the photogenerated charge carriers. After irradiation, holes accumulated in the VB of $TiO_2$ migrate into the PSi VB (process H, Figure 6), thus decreasing radiative recombination and PL intensity. This process should be very intense in the depletion region of $TiO_2$ and should significantly decrease surface recombination.

## CONCLUSIONS

In summary, $TiO_2$/PSi nanostructures were fabricated using metal-assisted chemical etching and atomic layer deposition. The crystalline structures, chemical compositions, and morphologies of the prepared and annealed $TiO_2$/PSi nanostructures were established. The approximate size of $TiO_2$ nanocrystals inside the PSi matrix was estimated using TEM and Raman spectroscopy. By controlling the number of deposition cycles, the size of anatase nanocrystallites inside the PSi matrix could be controlled. Optical and photoluminescence properties of $TiO_2$/PSi nanostructures are tailored by their structural parameters. The mechanisms of the PL emissions were discussed. Analysis of the PL spectra indicates PL quenching is due to electron−hole separation at the $TiO_2$/PSi heterojunction. Combining the large effective surface area of $TiO_2$/PSi nanostructures with fast charge carrier separation allows for improvement in the performance of photocatalysis, biosensors, and other optoelectronic devices.

## ASSOCIATED CONTENT

### Supporting Information

Plane-view SEM images and EDX analysis of the surface of prepared samples, cross-sectional SEM view of an individual pore, cross-sectional TEM images of the $TiO_2$ layer on the planar silicon surface, TEM images of PSi/$TiO_2$ nanostructures, Raman spectra of prepared ALD $TiO_2$ layers on the planar silicon surface, and high resolution XPS core level spectra of O 1s PSi/$TiO_2$ before and after annealing. This material is available free of charge via the Internet at http://pubs.acs.org.

## AUTHOR INFORMATION

### Corresponding Author

*E-Mail: yatsunskiy@gmail.com.

### Notes

The authors declare no competing financial interest.

## ACKNOWLEDGMENTS

Financial support from the National Centre for Research and Development under research grant "Nanomaterials and their Application to Biomedicine", Contract No. PBS1/A9/13/2012, is gratefully acknowledged.

## REFERENCES

(1) Avasthi, S.; McClain, W. E.; Man, G.; Kahn, A.; Schwartz, J.; Sturm, J. C. Hole-blocking Titanium-Oxide/Silicon Heterojunction and its Application to Photovoltaics. *Appl. Phys. Lett.* **2013**, *102*, 203901.

(2) Hu, S.; Shaner, M. R.; Beardslee, J. A.; Lichterman, M.; Brunschwig, B.; Lewis, N. Amorphous $TiO_2$ Coatings Stabilize Si, GaAs, and GaP Photoanodes for Efficient Water Oxidation. *Science* **2014**, *6187*, 1005−1009.

(3) Jian, S.; Xudong, W. Hierarchical $TiO_2$−Si Nanowire Architecture with Photoelectrochemical Activity under Visible Light Illumination. *Energy Environ. Sci.* **2012**, *5*, 7918−7922.



DOI: 10.1021/acs.jpcc.5b01670
J. Phys. Chem. C XXXX, XXX, XXX−XXX

(4) Yun, J. H.; Boukai, A.; Yang, P. High Density n-Si/n-$TiO_2$ Core/Shell Nanowire Arrays with Enhanced Photoactivity. *Nano Lett.* **2009**, *9*, 410−415.
(5) Takabayashi, S.; Nakamura, R.; Nakato, Y. A Nano-modified Si/$TiO_2$ Composite Electrode for Efficient Solar Water Splitting. *J. Photochem. Photobiol., A* **2004**, *166*, 107−113.
(6) Arakelyan, V. M.; Martirosyan, Kh. S.; Galstyan, V. E.; Shahnazaryan, G. E.; Aroutiounian, V. M. Room Temperature Gas Sensor Based on Porous Silicon/Metal Oxide Structure. *Phys. Status Solidi C* **2007**, *4*, 2059−2062.
(7) Lotfabad, E. M.; Kalisvaart, P.; Cui, K.; Kohandehghan, A.; Kupsta, M.; Olsena, B.; Mitlin, D. ALD $TiO_2$ Coated Silicon Nanowires for Lithium Ion Battery Anodes with Enhanced Cycling Stability and Coulombic Efficiency. *Phys. Chem. Chem. Phys.* **2013**, *15*, 13646.
(8) Wei, Z.; Li, R.; Huang, T.; Yu, A. Fabrication and Electrochemical Properties of Si/$TiO_2$ Nanowire Array Composites as Lithium Ion Battery Anodes. *J. Power Sources* **2013**, *238*, 165−172.
(9) Yan, D.; Bai, Y.; Yu, C.; Li, X.; Zhang, W. A Novel Pineapple-structured Si/$TiO_2$ Composite as Anode Material for Lithium Ion Batteries. *J. Alloys Compd.* **2014**, *609*, 86−92.
(10) Li, J.; Sailor, M. J. Synthesis and Characterization of a Stable, Label-free Optical Biosensor from $TiO_2$-coated Porous Silicon. *Biosens. Bioelectron.* **2014**, *55*, 372−378.
(11) Karacali, T.; Hasar, U. C.; Ozbek, I. Y.; Oral, E. A.; Efeoglu, H. Novel Design of Porous Silicon Based Sensor for Reliable and Feasible Chemical Gas Vapor Detection. *J. Lightwave Technol.* **2013**, *31*, 295−305.
(12) Huang, Z.; Geyer, N.; Werner, P.; de Boor, J.; Gösele, U. Metal-Assisted Chemical Etching of Silicon: A Review. *Adv. Mater.* **2011**, *23*, 285−308.
(13) Nam, T.; Kim, J. M.; Kim, M. K.; Kim, H. Low-temperature Atomic Layer Deposition of $TiO_2$, $Al_2O_3$, and ZnO Thin Films. *J. Korean Phys. Soc.* **2011**, *59*, 452−457.
(14) Iatunskyi, I.; Kempinski, M.; Jancelewicz, M.; Załeski, K.; Jurga, S.; Smyntyna, V. Structural and XPS Characterization of ALD $Al_2O_3$ Coated Porous Silicon. *Vacuum* **2015**, *113*, 52−58.
(15) Chartier, C.; Bastide, S.; Lévy-Clément, C. Metal-Assisted Chemical Etching of Silicon in HF−$H_2O_2$. *Electrochim. Acta* **2008**, *53*, 5509−5516.
(16) Šćepanović, M. J.; Grujić-Brojčin, M.; Dohčević-Mitrović, Z. D.; Popović, Z. V. Characterization of Anatase $TiO_2$ Nanopowder by Variable-Temperature Raman Spectroscopy. *Sci. Sintering* **2009**, *41*, 67−73.
(17) Mazza, T.; Barborini, E.; Piseri, P.; Milani, P.; Cattaneo, D.; Bassi, A. Li.; Bottani, C. E. Raman Spectroscopy Characterization of $TiO_2$ Rutile Nanocrystals. *Phys. Rev. B* **2007**, *75*, 045416.
(18) Choi, H. C.; Jung, Y. M.; Kim, S. B. Size Effects in the Raman Spectra of $TiO_2$ Nanoparticles. *Vib. Spectrosc.* **2005**, *37*, 33−38.
(19) Zhu, K. R.; Zhang, M. S.; Chen, Q.; Yin, Z. Size and Phonon-Confinement Effects on Low-Frequency Raman Mode of Anatase $TiO_2$ Nanocrystal. *Phys. Lett. A* **2005**, *340*, 220−227.
(20) Chaaya, A. A.; Viter, R.; Baleviciute, I.; Bechelany, M.; Ramanavicius, A.; Gertnere, Z.; Erts, D.; Smyntyna, V.; Miele, P. Tuning Optical Properties of $Al_2O_3$-ZnO Nanolaminates Synthesized by Atomic Layer Deposition. *J. Phys. Chem. C* **2014**, *118*, 3811−3819.
(21) Chaaya, A. A.; Viter, R.; Bechelany, M.; Alute, Z.; Erts, D.; Zalesskaya, A.; Kovalevskis, K.; Rouessac, V.; Smyntyna, V.; Miele, P. Evolution of Microstructure and Related Optical Properties of ZnO Grown by Atomic Layer Deposition. *Beilstein J. Nanotechnol.* **2013**, *4*, 690−698.
(22) Reddy, K. M.; Manorama, S. V.; Reddy, A. R. Bandgap Studies on Anatase Titanium Dioxide Nanoparticles. *Mater. Chem. Phys.* **2002**, *78*, 239−245.
(23) Chaaya, A. A.; Viter, R.; Baleviciute, I.; Bechelany, M.; Ramanavicius, A.; Erts, D.; Smyntyna, V.; Miele, P. Optical and Structural Properties of $Al_2O_3$/ZnO Nanolaminates Deposited by ALD Method. *Phys. Status Solidi C* **2014**, *11*, 1505−1508.
(24) Krishna, M. G.; Rao, K. N.; Mohan, S. Optical Properties of Ion Assisted Deposited Zirconia Thin Films. *J. Vac. Sci. Technol., A* **1992**, *10*, 3451−3455.
(25) Arenas, M. C.; Hu, H.; Nava, R.; del Rio, J. A. Determination of the Complex Refractive Index of Porous Silicon Layers on Crystalline Silicon Substrates. *Int. J. Mod. Phys. B* **2010**, *24*, 4835.
(26) Pap, A. E.; Kordas, K.; Vahakangas, J.; Uusimaki, A.; Leppavuori, S.; Pilon, L.; Szatmari, S. Optical Properties of Porous Silicon. Part III: Comparison of Experimental and Theoretical Results. *Opt. Mater.* **2006**, *28*, 506−513.
(27) Yenchalwar, S. G.; Azhagan, V. K.; Shelke, M. V. Enhanced Photoluminescence and Photoactivity of Plasmon Sensitized nSiNWs/$TiO_2$ Heterostructures. *Phys. Chem. Chem. Phys.* **2014**, *16*, 17786.
(28) Kernazhitsky, L.; Shymanovska, V.; Gavrilko, T.; Naumov, V.; Fedorenko, L.; Kshnyakin, V.; Baran, J. Room Temperature Photoluminescence of Anatase and Rutile $TiO_2$ Powders. *J. Lumin.* **2014**, *146*, 199−204.
(29) Choudhury, B.; Choudhury, A. Tailoring Luminescence Properties of $TiO_2$ Nanoparticles by Mn Doping. *J. Lumin.* **2013**, *136*, 339−346.
(30) Akhavan, O.; Ghaderi, E.; Rahimi, K. Adverse Effects of Graphene Incorporated in $TiO_2$ Photocatalyst on Minuscule Animals under Solar Light Irradiation. *J. Mater. Chem.* **2012**, *22*, 23260.
(31) Nasr, M.; Chaaya, A. A.; Abboud, N.; Bechelany, M.; Viter, R.; Eid, C.; Khoury, A.; Miele, P. Photoluminescence: a Very Sensitive Tool to Detect the Presence of Anatase in Rutile Phase Electrospun $TiO_2$ Nanofibers. *Superlattices Microstruct.* **2014**, *77*, 18−24.
(32) Chang, Y. H.; Liu, C. M.; Chen, C.; Cheng, H. E. The Effect of Geometric Structure on Photoluminescence Characteristics of 1-D TiO2 Nanotubes and 2-D $TiO_2$ Films Fabricated by Atomic Layer Deposition. *J. Electrochem. Soc.* **2012**, *159*, 401−405.
(33) Das, K.; Sharma, S. N.; Kumar, M.; De, S. K. Morphology Dependent Luminescence Properties of Co Doped $TiO_2$ Nanostructures. *J. Phys. Chem. C* **2009**, *113*, 14783−14792.
(34) Abazovic, N. D.; Comor, M. I.; Dramicanin, M. D.; Jovanovic, D. I.; Ahrenkiel, S. P.; Nedeljkovic, J. M. Photoluminescence of Anatase and Rutile $TiO_2$ Particles. *J. Phys. Chem. B* **2006**, *110*, 25366−25370.
(35) Zhang, J.; Chen, X.; Shen, Y.; Li, Y.; Hu, Z.; Chu, J. Synthesis, Surface Morphology, and Photoluminescence Properties Anatase Iron-Doped Titanium Dioxide Nano-crystalline Films. *Phys. Chem. Chem. Phys.* **2011**, *13*, 13096−13105.
(36) Jun, J.; Jin, C.; Kim, H.; Kang, J.; Lee, C. The Structure and Photoluminescence Properties of $TiO_2$-coated ZnS Nanowires. *Appl. Phys. A: Mater. Sci. Process.* **2009**, *96*, 813−818.
(37) Knorr, F. J.; Zhang, D.; McHale, J. L. Influence of $TiCl_4$ Treatment on Surface Defect Photoluminescence in Pure and Mixed-Phase Nanocrystalline $TiO_2$. *Langmuir* **2007**, *23*, 8686−8690.
(38) Zhao, J.; Jia, C.; Duan, H.; Li, H.; Xie, E. Structural Properties and Photoluminescence of $TiO_2$ Nanofibers were Fabricated by Electrospinning. *J. Alloys Compd.* **2008**, *461*, 447−450.
(39) Zhang, W. F.; Zhang, M. S.; Yin, Z.; Chen, Q. Photoluminescence in Anatase Titanium Dioxide Nanocrystals. *Appl. Phys. B: Lasers Opt.* **2000**, *70*, 261−265.
(40) Wang, X.; Feng, Z.; Shi, J.; Jia, G.; Shen, S.; Zhouab, J.; Li, C. Trap States and Carrier Dynamics of $TiO_2$ Studied by Photoluminescence Spectroscopy under Weak Excitation Condition. *Phys. Chem. Chem. Phys.* **2010**, *12*, 7083−7090.


DOI: 10.1021/acs.jpcc.5b01670
J. Phys. Chem. C XXXX, XXX, XXX−XXX